



Catalyst layer cracks by buckling deformation of membrane electrode assemblies under humidity cycles and mitigation methods



Tomoaki Uchiyama*, Hideyuki Kumei, Toshihiko Yoshida

Toyota Motor Corporation, Fuel Cell System Development Div., R&D Group 1, 1200, Mishuku, Susono, Shizuoka 410-1193, Japan

HIGHLIGHTS

- Catalyst layer cracks occurred by a bulge deformation of membrane electrode assemblies with repeated humidity cycles.
- Formation of catalyst layer cracks was delayed in lower clearance heights.
- In FEM simulation, larger stresses happened in the region of the CL crack occurrence in the experiments.
- An in-plane swelling of the PEM was reduced in lower clearance heights.

ARTICLE INFO

Article history:

Received 22 February 2013

Received in revised form

26 March 2013

Accepted 8 April 2013

Available online 18 April 2013

Keywords:

Mechanical degradation

Catalyst layer crack

Swelling

Clearance height

In-plane buckling

Fuel cells

ABSTRACT

In this study, the formation of catalyst layer (CL) cracks in a membrane electrode assembly (MEA) under multiple humidity cycles is analyzed to propose solutions to mitigate the crack formation. The MEA is fabricated by the thermal transfer of catalyst layers (4 μm thickness) to both sides of the NR211 (25 μm thickness). The buckling deformations are created by microscopic 300 μm diameter holes in the polyimide (PI) films. The microscopic holes model the clearance between the MEA and gas diffusion layers (GDLs). The clearance height is adjusted by the film thickness. The MEA and PI film are sandwiched between the GDLs and exposed to humidity cycles in test cells. When the clearance height decreases, the CL cracks do not tend to develop after repeated humidity cycles. In the FEM analysis, swelling of the NR211 causes large plastic strains on the CL in areas that correspond to crack locations in the experiment. For the lower clearance heights, the plastic strain in the CL is reduced due to reduction of the in-plane swelling ratio of the NR211 as it swells. A reduction in in-plane swelling of the PEM by thoughtful structure design is directly effective in preventing CL cracks as well.

© 2013 Elsevier B.V. All rights reserved.

1. Introduction

It is hoped that fuel cell (FC) vehicles using polymer electrolyte fuel cells (PEFCs) will become widespread because they are highly-efficient, zero-emission vehicles. The current generation already has adequate performance and durability, and the next technical challenge is to reduce their production cost. This requires modifications to the materials of the membrane electrode assemblies (MEAs) and gas diffusion layers (GDLs). Improvements to the properties of the polymer electrolyte membrane (PEM) are one of the most effective methods to obtain better electricity generation, especially under dry and hot operating conditions, and to reduce costs [1]. Although higher proton conductivity of the PEM would directly contribute to improved generation in low-humidity

conditions, this method could cause large swelling when the PEM is exposed to increased humidity. As a result, the dimensional stability of the MEA under multiple humidity cycles is decreased. Creating a thinner PEM is a practical method to achieve higher proton conductivity [1]; however, even the normally designed PEM accelerates the formation of membrane pinholes. Therefore, dimensional instabilities and use of a thinner PEM to increase proton conductivity will decrease the mechanical durability of the MEA [1] and consequently reduce generating performance and fuel economy in long-term use. In order to support proton conductivity and PEM durability at the same time, new solutions for MEA properties are required and should be based on mitigating the degradation mechanism.

The PEM is degraded by mechanical deformation [1–21] and radicals created by chemical reactions [1,19–26]. In this paper, the mechanical degradation mechanism is discussed. The degradation mechanism under repeated humidity cycles has been previously

* Corresponding author. Tel.: +81 55 997 9078; fax: +81 55 997 7120.

E-mail address: tomoaki@uchiyoama.tec.toyota.co.jp (T. Uchiyama).

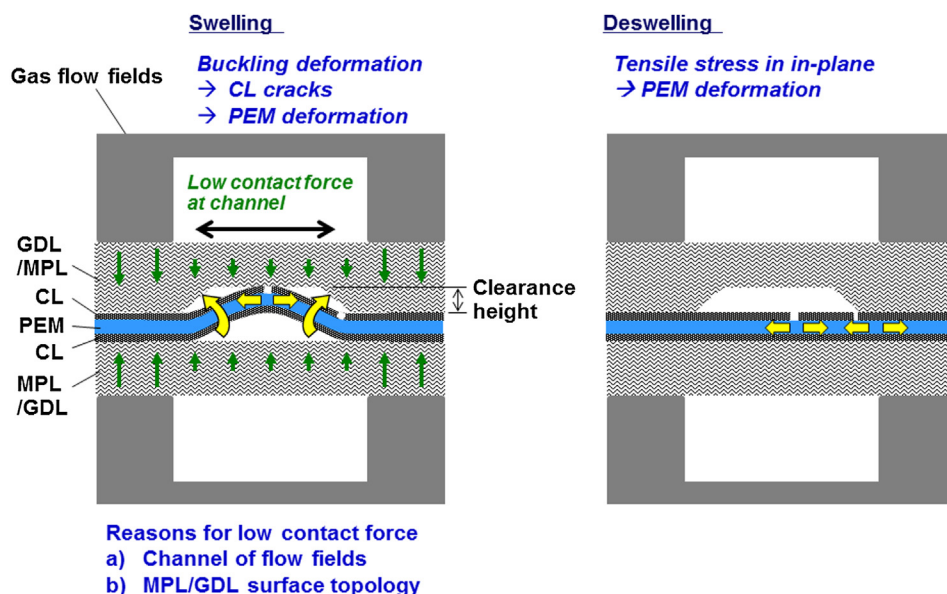


Fig. 1. Proposed mechanical degradation mechanism of membrane electrode assemblies under multiple humidity cycles.

discussed [2–15,18,19], and a new mechanical degradation mechanism, i.e., wrinkle deformations with in-plane buckling under swelling, was proposed by the author as described in Fig. 1 [16,17]. Under higher humidity conditions in the FCs, the MEA buckles into sections where the contact pressure is zero. The absence of contact pressure means that there are clearances of several hundred micrometers between the MEA and the microporous layer (MPL)/GDL. In fact, the clearances occur under channel portions of the gas flow fields due to the low compressive force [27], which is influenced by the GDL fiber texture and the wavy MPL surface shapes [28,29]. Repeated humidity cycles generate cracks in the catalyst layer (CL) by strain accumulation [17,30]. Moreover, swelling and deswelling cycles cause PEM plastic deformation under the CL cracks, which results in pinholes and tears in the PEM or thinning of the PEM [2,17].

The ultimate goal in this paper is to obtain solutions to suppress the formation of CL cracks. First, a buckling test of the MEA under repeated humidity cycles is carried out. The clearances are set at a diameter of 300 μm in the polyimide film by laser processing. Here, clearance describes the interspace between the MEA and the MPL/GDL and corresponds to the surface topology of the MPL and GDL [28,29]. Next, stress/strain behaviors seen in the buckling test are simulated with a finite element method (FEM) by using a previously described method [17]. The FEM analysis of the MEA under humidity changes is effective in estimating the stress/strain behavior [2,3,7–13,15,17] because direct measurement of the MEA's deformation is relatively difficult. Through these experiments and simulations, the effects of the clearance height on CL crack formation are investigated, and a mechanism to suppress formation of the cracks is considered. A lower swelling ratio of the PEM is also analyzed to study its advantages. Finally, desirable properties of the MEA and GDL are proposed that will mitigate CL crack formation.

2. Experimental procedures

2.1. Materials

The NR211, which is a perfluorosulfonic acid membrane, was used in all experiments. This PEM is a commercial product also known as Nafion[®]. The nominal equivalent weight is 1100 g mol⁻¹ of sulfonic group, and membrane thickness is 25 μm . The catalyst ink was prepared by mixing 60 wt.% Pt/C and Nafion[®] ionomer

solution with 1/1 weight ratio of each solute. The ink was coated onto a Teflon sheet with a Pt loading of 0.2 mg cm⁻². The formed CLs were transferred to both sides of the NR211 using the heat press method at 3 MPa and 130 °C for 10 min to make NR211–CL. The corresponding CL was approximately 4.0 μm in thickness, and the whole NR211–CL was 33 μm thick. Carbon paper (TGP-H-060, Toray) containing a microporous layer (MPL) on one side was used as the GDL on both the anode and cathode sides.

2.2. Buckling test of MEA

The NR211–CL membranes were laminated with polyimide (PI) film, sandwiched between the GDLs and fastened by gas flow fields at 150 N in the fuel cell (Fig. 2). Eight microscopic holes of 300 μm diameter were manufactured in the film by laser processing. The clearance size can be variable between the MEA and GDL and clearances with width in a few hundreds micrometer exist in FCs [28]. It is obvious that the NR211–CL buckles at microscopic holes of diameter over 190 μm , which is an estimated minimum diameter for buckling [16]. The clearance of 300 μm , which is larger than 190 μm , was adopted in this study to cause buckling of the NR211–CL with certainty.

The clearances were adjusted by changing the PI film thickness. Film thicknesses of 100, 62.5, 37.5 and 25.0 μm were prepared. In our previous study, the MEA showed wrinkle deformations by the

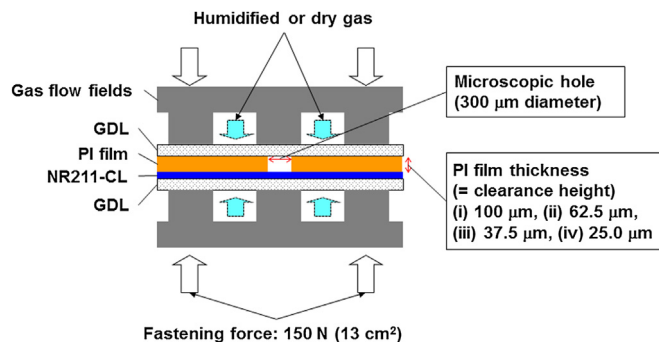


Fig. 2. Diagram of a buckling test in the membrane electrode assemblies under multiple humidity cycles.

Table 1
Material properties for FEM simulation.

Material	Mechanical properties			Swelling properties
	Approximation type	Stress–strain correlation	Poisson ratio	
NR211	Linear elastic, plastic with isotropic hardening	Isotropic, Fig. 3(a)	$\nu = 0.40$	Fig. 4
CL	Linear elastic, perfectly plastic	Isotropic, Fig. 3(b)	$\nu = 0.25$	No swelling
GDL	Linear elastic	Anisotropic, $E_r = E_0 = 1000$ MPa, $E_z = 20$ MPa	$\nu = 0.13$	No swelling
PI	Linear elastic	Isotropic, $E = 2$ GPa	$\nu = 0.30$	No swelling

in-plane swelling under humidity cycles at low contact pressure of 0.08 MPa between the MEA and GDL [16]. Height of the wrinkle deformation after humidity cycles exceeded 50 μm (value is not shown in the article). Much higher clearances could be created by pushing the GDL outside in thickness direction during swelling of the MEA. Therefore, it is presumed that the height of 100 μm exists during swelling. The clearance heights become lower at higher contact pressure.

The active area subjected to the humidity cycles was 13 cm^2 . The test cell temperature was controlled at 80 $^\circ\text{C}$ by circulating hot water in the fuel cells. Humidified N_2 gas and dry N_2 gas were alternately and repeatedly supplied to the cell for 1 min and 2 min, respectively. Based on resistance measurements of the NR211–CL, values of the relative humidity (RH) were 100 RH% (in liquid water) at a humidified condition and 5 RH% at a dry condition. The resistance of the NR211–CL under these humidity cycles was measured as a combination of the NR211–CL and the GDL without the PI film in the fuel cells. After five cycles and then every 1000 cycles, the GDL on the PI film was taken from the samples, and the CL surfaces in the microscopic holes were observed by laser microscope (VK-8500, Keyence, Japan) at 25 $^\circ\text{C}$, 50 RH% to confirm the formation of CL cracks. After the test, several samples were removed from the PI film and were exposed to palladium sputtering. The samples were observed in a scanning electron microscope (SEM, VE-7800, Keyence, Japan) to describe the CL surface state on the topside bulges. It should be noted that there were no cracks on the CL before the buckling test based on observations of the CL surface.

3. FEM analysis model for MEA buckling test

3.1. Material properties

The material properties used in the FEM simulation of the buckling test are listed in Table 1. These properties are quoted from Ref. [17]. The mechanical properties of the NR211 and NR211–CL were measured by tensile tests, and parameters for the elastoplastic properties of the NR211 and CL were determined from

stress–strain correlations at each relative humidity at 80 $^\circ\text{C}$ [17]. Tensile tests of the NR211 itself were carried out, and the approximated stress–strain properties are summarized in Fig. 3(a). Mechanically, the properties of the CL are defined as linear elastic and perfectly plastic. Because the isolated CL was not analyzed by the tensile test, the parameters of the CL are determined from data for the NR211 and NR211–CL. Approximated stress–strain properties of the CL are shown in Fig. 3(b).

The CL cracks occur during tensile test of the NR211–CL [30]. The number of cracks increases and these widths expand with increasing tensile strain. Nafion ionomer in the CL shows elastoplasticity just like Nafion membrane. After yielding of the ionomer, the visible cracks occur in the CL during the tensile test. In other words, the cracks would occur after plastic deformation in the CL. The crack initiation on the CL properties should be introduced to physically simulate the crack formation in the FEM. However, we do not have a crack initiation data in the liquid water. Therefore, the crack initiation properties are not used in present paper.

Swelling ratios of the NR211 are defined in the in-plane and through-plane directions. In-plane swelling (ϵ_{in}) was found to be 12.7%, and through-plane swelling (ϵ_{th}) was 24.6%. From the measurement data at 100 RH% (in liquid water), the NR211's swelling behavior was calculated by correlating the dimensional change with the relative humidity [3] (Fig. 4). In this paper the swelling ratio in 100 RH% means that in liquid water. Additionally, we define a second case wherein ϵ_{in} is 5.0% and ϵ_{th} is 43.5% so as to investigate the result of reducing the in-plane swelling. The volume increase of this swelling case is equivalent to that of the NR211 (58.2%). In all simulation cases, the CL and GDL do not swell with increased humidity.

3.2. Analysis model

A FEM analysis is useful to calculate stress–strain behaviors seen in the NR211–CL buckling test. In the simulation, the material properties of the NR211 and CL become altered with humidity changes, and bulge deformations of the NR-211 can take place just

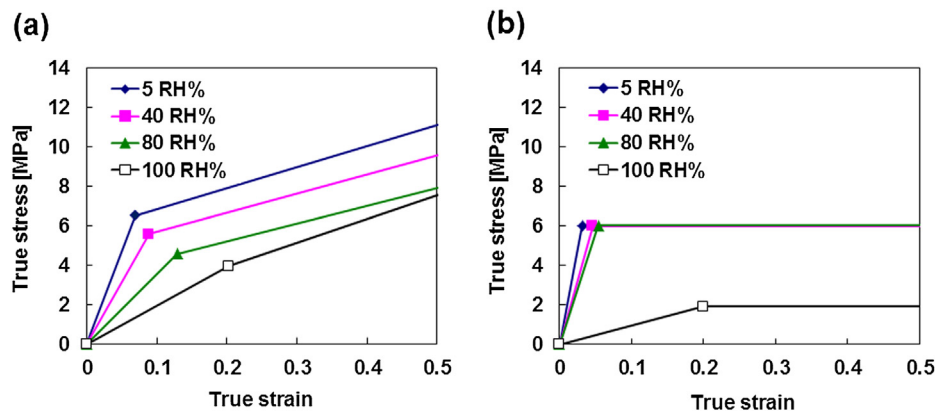


Fig. 3. Approximated mechanical properties of (a) NR211 and (b) the catalyst layer (CL) under several relative humidities.

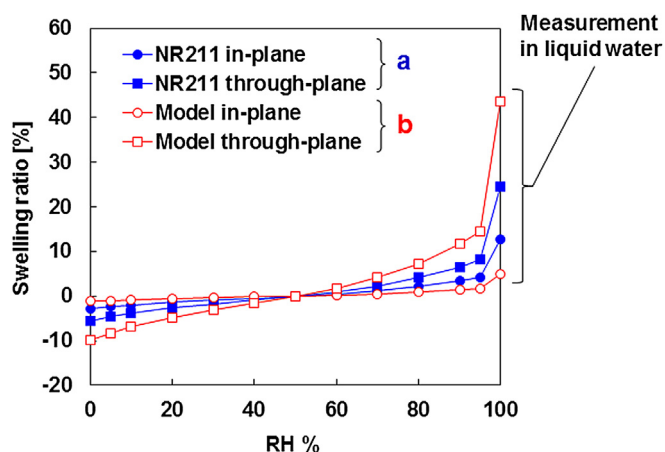


Fig. 4. Dimensional changes of the NR211 and the modeled PEM with relative humidity changes.

as in the buckling experiments. The FEM analysis was conducted using the commercial software ABAQUS®. An axisymmetric model is used for the simulation of the buckling test (Fig. 5). The clearance diameter in the PI film was 300 μm , and the clearance height between the CL and GDL was set at 100, 62.5, 37.5 and 10.0 μm . Eight-node axisymmetric elements (CAX8) were used to mesh the components of the NR211 and CL. Four-node axisymmetric elements (CAX4) or three-node axisymmetric elements (CAX3) were used for the PI film and GDLs. The gas flow fields were replaced by rigid bodies, and the MPL was neglected.

The boundary condition $u_z = 0$ was applied to the bottom rigid body, and $u_r = 0$ was assigned to the right-hand side of all components of the body (u_i represents the deformation in the i

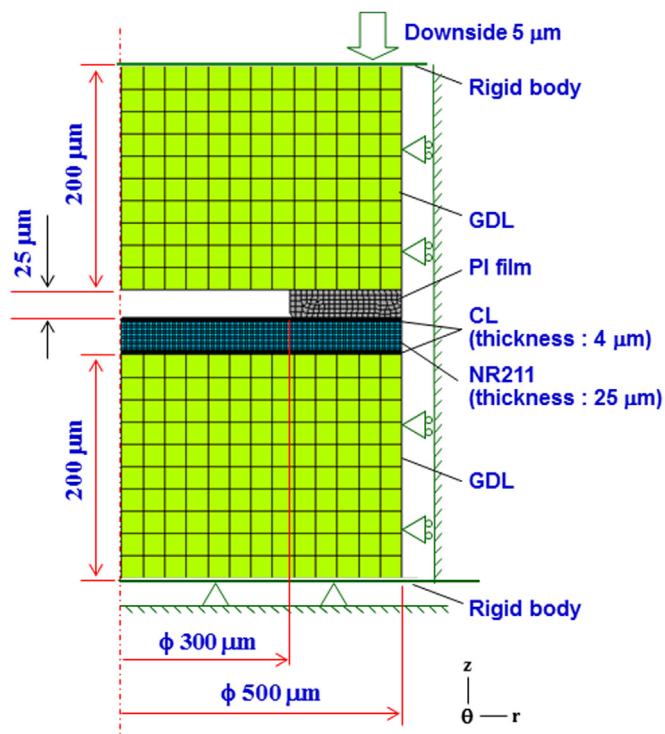


Fig. 5. Axisymmetric FEM model for the buckling test of the NR211–CL. The PI film thickness is drawn as 25 μm in this figure. Values of 100, 62.5, 37.5 and 10 μm were also considered.

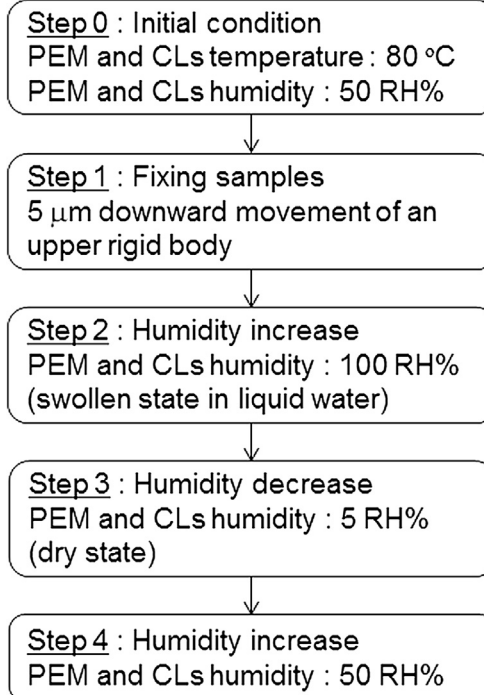


Fig. 6. FEM analysis procedures for simulating the NR211–CL buckling test.

direction); these conditions are depicted in Fig. 5. The interfaces between the NR211 and CLs were bonded with no slip allowed. Other interfaces in the model were not bonded, and friction was neglected (zero).

The FEM analysis procedures are presented in Fig. 6. The humidity changes follow those found in NR211 during the buckling test. Dimensional changes of the NR211 due to relative humidity and temperature changes are simulated by control of both thermal coefficients and temperature changes. Initially, the NR211 and CLs are in a 50 RH% atmosphere (Step 0). To affix the NR211–CL, PI film and GDLs and to approximate the experiment conditions (Fig. 2), an upper rigid body pushes downward at 5 μm , and 0.12 MPa of contact pressure are added to the NR211–CL (Step 1). The humidity rises to 100 RH% (in liquid water) (Step 2), decreases to 5 RH% (Step 3) and finally returns to 50 RH% (Step 4). The humidity in the NR211 and CL changed uniformly. Deformations and stress–strain behaviors of the NR211–CL were calculated through this procedure.

4. Results

4.1. Buckling test of MEA under repeating humidity cycles

The NR211–CL was exposed to humidity cycles so as to investigate the formation of CL cracks at controlled clearances between the CL and GDL. Eight bulging sections of the NR211–CL were observed after 5 cycles and every 1000 cycles. The CL cracks that formed on the central and topside portions were checked with the laser microscope. A flaw that is visible from the surface and is more than 5 μm length is defined as a crack. The number of bulges that proceeded to the CL crack stage is summarized in Table 2. It is evident that cracks do not tend to happen at lower clearance heights.

The NR211–CL was separated from the PI film after the humidity cycles, and the bulge deformations of the NR211–CL were observed by SEM. An example of a bulge at 100 μm clearance height after 5 cycles was captured from an oblique viewpoint and is presented in

Table 2
Occurrence of catalyst layer cracks.

PI film thickness [μm]	Humidity cycles			
	5	1000	2000	8500
100	8	8	N.D. ^a	N.D.
62.5	4	7	N.D.	N.D.
37.5	N.D.	0	1	N.D.
25.0	N.D.	0	0	0

Eight points are observed.

^a N.D. indicates observation is not carried out.

Fig. 7. The NR211–CL has bulged out into the clearances due to plastic deformation, which is caused by in-plane buckling during swelling. We observe that the CL does not come into contact with the MPL during NR211–CL hydration because signatures such as friction with the MPL or attachments between the MPL and the CL are not found. Therefore, the NR211–CL deforms without restriction from the MPL during NR211–CL hydration. The extent of the bulge deformation is evaluated by the index of the bulge strain as described in a previous article [16]. The bulge strain at 100 μm clearance height was calculated by Eq. (1) and is 0.011.

$$\text{Bulge strain} = \frac{\text{Bulge length} - \text{Bulge width}}{\text{Bulge width}} \quad (1)$$

This value is used for comparison with simulation data in Section 5.1. This bulge showed an average bulge strain in 8 bulges. This deformation is appropriate for comparing with simulation one, because this was adequately exposed to humidity cycles.

Basically, the CL cracks emerge at the central and topside portions as shown in Fig. 8. The cracks can be seen inside the round dotted-line in the SEM image. Higher magnification images were captured by SEM, and representative images are displayed in Fig. 9. These images are focused on the center of the bulge, and the cracks have clearly taken place in these sections. Although the cracks can be found at 100, 62.5 and 37.5 μm thicknesses within 2000 cycles, the cracks do not occur at 25.0 μm thickness after 8500 cycles. Emerged cracks are formed in an isotropic direction on the top of the bulge.

At a clearance height of 100 μm , the cracks occur within 5 cycles, and the length of the cracks is less than 20 μm . The cracks grow wider and begin to propagate in a longitudinal direction after 1000

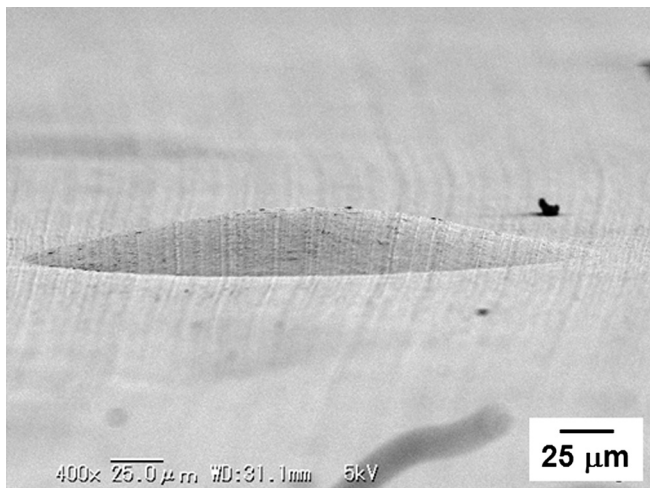


Fig. 7. A SEM observation of the NR211–CL bulge deformation after 5 humidity cycles at 100 μm clearance height. The deformation is captured from an oblique view.

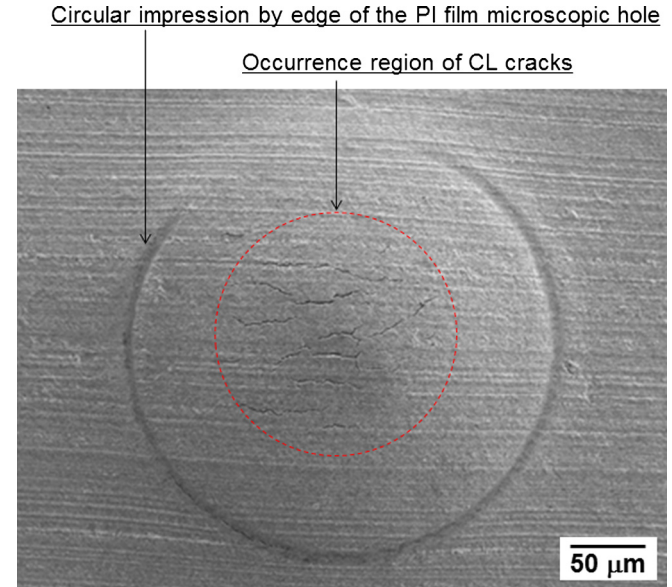


Fig. 8. A SEM observation from an upper surface of the NR211–CL bulge after 1000 humidity cycles at 100 μm clearance height.

cycles (Fig. 9(a)), and the length of the cracks becomes more than 30 μm .

The emerged cracks are narrower and the number of the cracks is fewer for the 62.5 μm (Fig. 9(b)) thick sample than the 100 μm thick sample after 1000 cycles (Fig. 9(a)). Only one out of eight bulges created the CL cracks after 2000 cycles in the 37.5 μm thick sample (Fig. 9(c)), and the cracks do not exceed a length of 10 μm . When the clearance height is 25.0 μm , no cracks are found after 8500 cycles, and friction signatures are recognizable (in center of picture, Fig. 9(d)). Likewise, signatures of friction or compression by the MPL are found on the CL in the 62.5 μm and 37.5 μm thick samples.

4.2. FEM analysis of MEA buckling test

The NR211–CL deformation and stress/strain behavior due to dimensional changes in NR211 under humidity cycling were analyzed using a FEM. The mechanical properties of the CL are elastoplastic, and the crack initiation and propagation in the CL are not defined. The formation of CL cracks is not simulated; instead, the level and distribution of the plastic strain in the CL are calculated in order to consider the possibility of CL crack formation in the experiment.

The deformation behaviors in a 100 μm clearance height sample are shown in Fig. 10. First, the adequacy of the simulation results in modeling the buckling experiment must be verified before reviewing simulation data. The bulge strain calculated by Eq. (1) at 50 RH% after one humidity cycle is 0.010 from Fig. 10(d). This strain is similar to the strain of 0.011 in the experiment (as stated previously), and possibility of the simulation validity was confirmed. Because the crack width is much narrower than the bulge length in the experiment, a good agreement was shown.

The contours in the components indicate the plastic strain in the radial direction. When the NR211 swells, the NR211–CL buckles into the clearances and is in a bending state (Fig. 10(b)). In particular, the upper bending portion in the CL is subjected to biaxial (radial and circumferential) tensile stress and shows higher plastic strain. When the NR211–CL are exposed to the dry state at 5 RH%, the bulges do not disappear perfectly (Fig. 10(c)), and the bulge

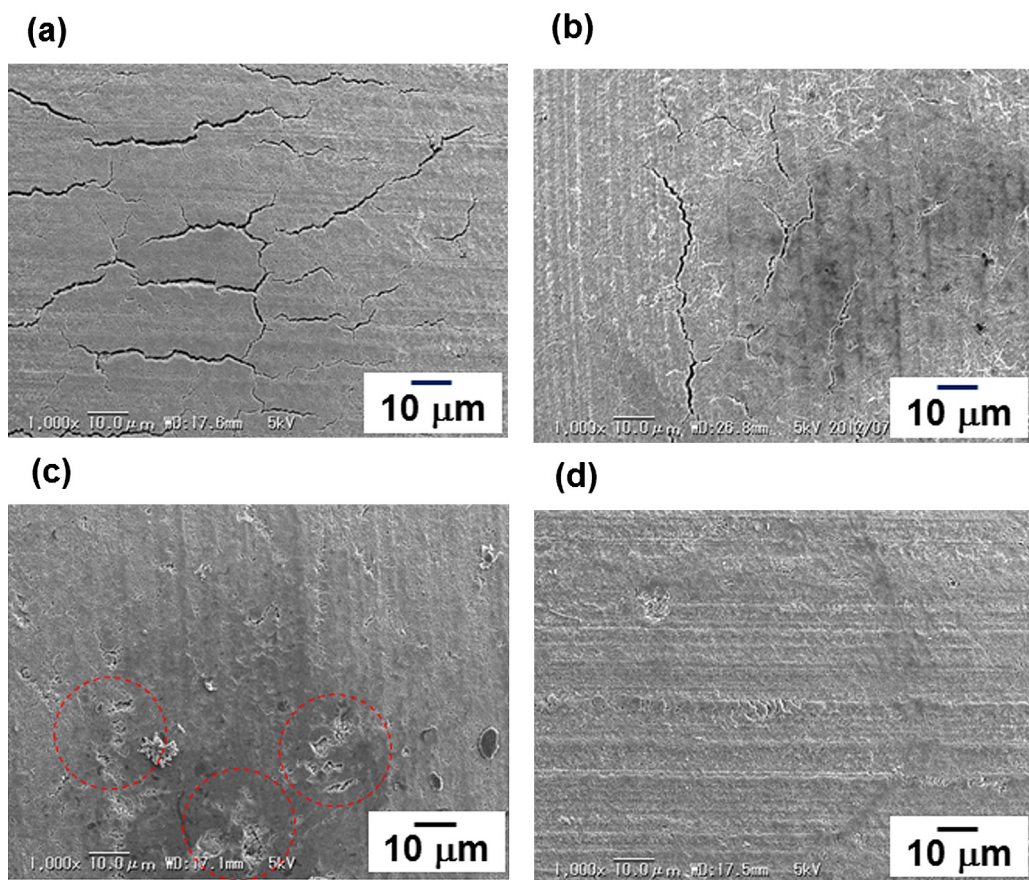


Fig. 9. SEM observations from an upper surface of the NR211–CL bulge (a) after 1000 cycles at 100 μm clearance height, (b) after 1000 cycles at 62.5 μm clearance height, (c) after 2000 cycles at 37.5 μm clearance height (CL cracks are circled) and (d) after 8500 cycles at 25.0 μm clearance height.

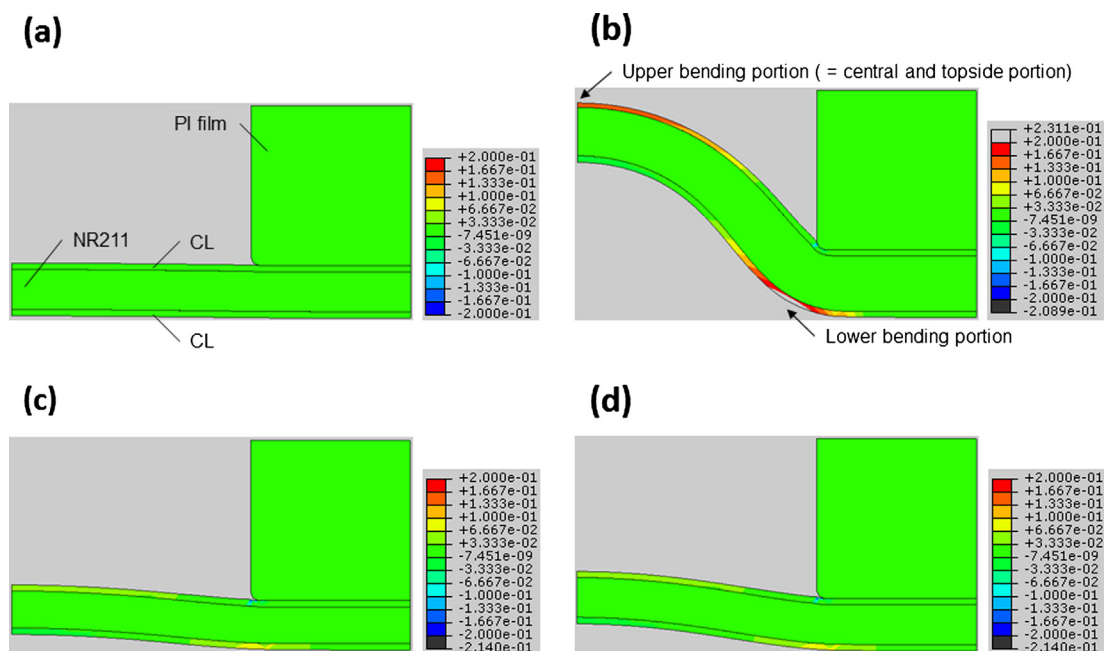


Fig. 10. Deformation behaviors of the NR211–CL at 100 μm clearance height during a humidity cycle. The contour indicates the plastic strain in radial direction. The conditions were (a) initial state at 50 RH%, (b) swelled state at 100 RH%, (c) dry state at 5 RH% and (d) return to initial state at 50 RH%.

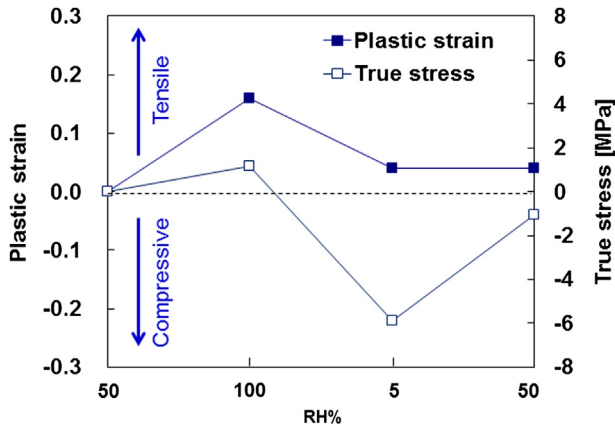


Fig. 11. Plastic strain and true stress behaviors at the central and topside portion of the CL versus relative humidity change at 100 μm clearance height. Radial and circumferential components are similar and are shown in this figure.

continues to exist at 50 RH% at the end of a humidity cycle (Fig. 10(d)). Remarkably, the plastic strain does not occur in the NR211 in either the swelled or dry states. Therefore, permanent deformation of the NR211–CL results from the plastic deformation of the CL.

The CL cracks occurred at the upper bending portion in the experiment as shown in Fig. 8. The following analyses are concerned with only the plastic strain at the upper bending portion (central and topside portion). The plastic strains and true stresses in the CL during a humidity cycle are shown in Fig. 11. The radial and

circumferential components are of similar value in this portion. When the NR211–CL was exposed to liquid water, the tensile stress and tensile plastic strain increased in the upper CL. When the NR211–CL was in the dry state, the plastic strain decreased because the CL was subjected only to compressive stress. The plastic strain is retained upon returning to the 50 RH% level. Consequently, the tensile plastic strain remains in the CL, and the NR211–CL shows a bulge shape.

The deformations of the NR211–CL under a humidity cycle were simulated for several clearance heights. The deformations of the NR211–CL at 100 RH% are summarized in Fig. 12, and the contour indicates the equivalent plastic strain level. Except the case of 100 μm clearance, the extent of the bulges was restricted by the upper GDL. Because the strains in the CL at the upper bending portion were distinguishable in all cases, the strain in the portion should be considered. Fig. 13 indicates the equivalent plastic strain in the CL at the upper bending portion during a humidity cycle for several sets of conditions. The most obvious difference among these conditions is the strain seen at 100 RH%, and it can be seen that the plastic strains decrease with a decrease in the clearance height at an in-plane swelling of 12.7%. No plastic strain occurs for the 10 μm clearance height.

The effect of the in-plane swelling of the PEM is investigated by adjusting the PEM dimensional changes with relative humidity. As shown in Fig. 4, the modeled PEM swelling ϵ_{in} is assumed to be 5.0%, and the stress–strain behaviors are calculated by the same method as for the basic swelling ratio ($\epsilon_{\text{in}} = 12.7\%$). No plastic strains happen within a humidity cycle in the case ϵ_{in} equal to 5.0% as is shown in Fig. 12(f) and Fig. 13 despite the clearance height of 100 μm .

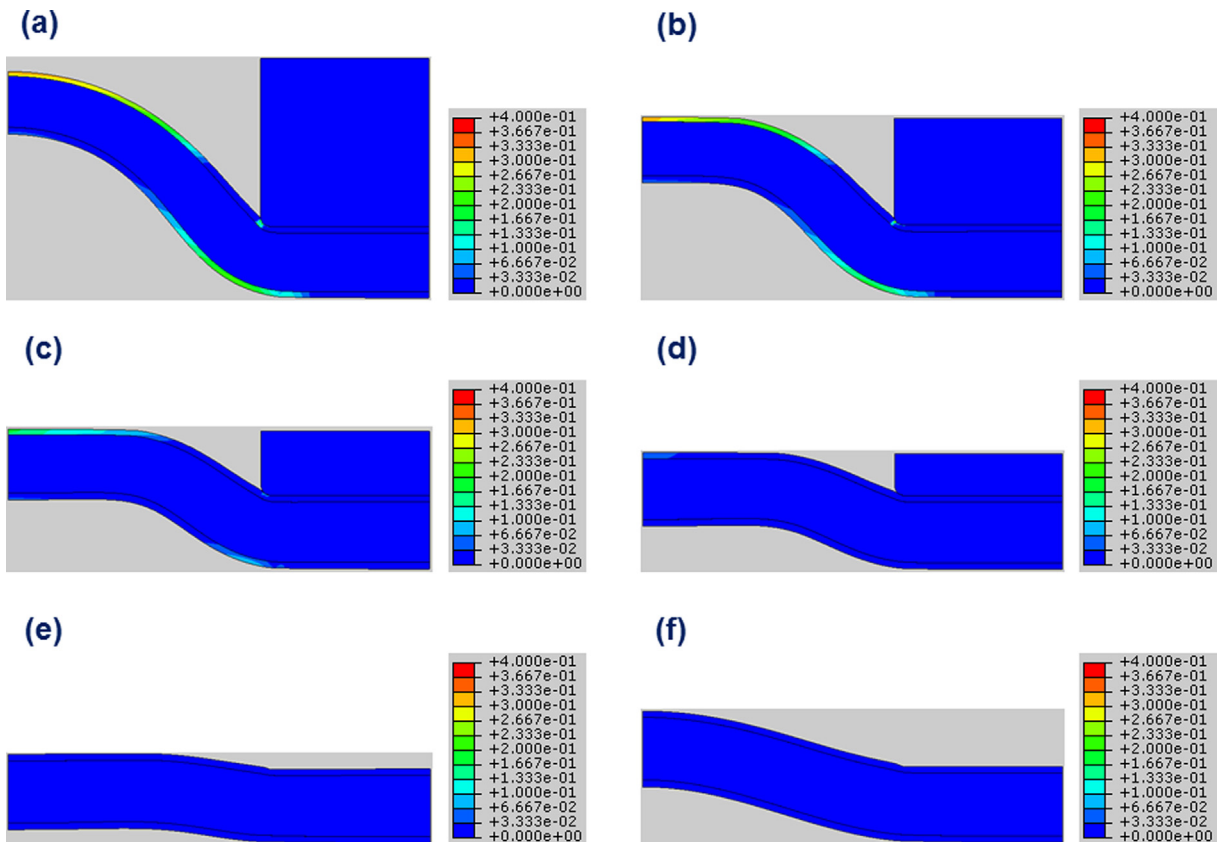


Fig. 12. Equivalent plastic strains at 100 RH% (swelled state) for chosen in-plane swelling ratios of the NR211 (ϵ_{in}) and clearance heights (h). (a) $\epsilon_{\text{in}} = 12.7\%$, $h = 100 \mu\text{m}$, (b) $\epsilon_{\text{in}} = 12.7\%$, $h = 62.5 \mu\text{m}$, (c) $\epsilon_{\text{in}} = 12.7\%$, $h = 37.5 \mu\text{m}$, (d) $\epsilon_{\text{in}} = 12.7\%$, $h = 25.0 \mu\text{m}$, (e) $\epsilon_{\text{in}} = 12.7\%$, $h = 10.0 \mu\text{m}$ and (f) $\epsilon_{\text{in}} = 5.0\%$, $h = 100.0 \mu\text{m}$.

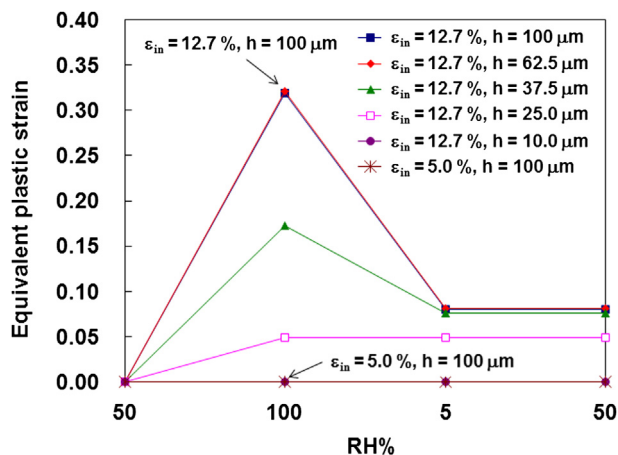


Fig. 13. Equivalent plastic strain behaviors of the CL at the upper bending portion during a humidity cycle.

5. Discussion

5.1. CL crack formation mechanism under humidity cycles in the buckling test

Due to repeated biaxial strains in the CL under multiple humidity cycles, the cracks propagate along the width and length directions through microstructure changes in the CL. The CL cracks generally resulted from failures in the Nafion ionomer or delamination between the ionomer and the carbon/Pt agglomerate [31]. Presumably, the cracks in the CL propagate in the lower ionomer-content regions of the CL and at pore sites.

In the buckling test of the NR211–CL, the CL is stable against crack formation when the clearance height is low (Table 2). Following this finding, the formation of cracks might also be delayed by using lower clearance heights in actual fuel cells. It is important to understand the mechanism that allows delay of CL crack formation in the lower clearance height samples. In the FEM simulation that models the NR211–CL buckling test, the plastic strain in the CL is at a decreased level at the lower clearance heights (Figs. 12 and 13). It should be noted that CL crack formation in the experiment tends to be related to the plastic strain in the CL in its swollen state in the simulation. Because the plastic

strain in the dry state (5 RH%) is not much different among clearances (Fig. 13), the compressive stress while relaxing does not affect CL crack formation. Therefore, reduction of the strain in the CL in the swollen state of the NR211–CL is effective in delaying CL crack formation.

We focused on the deformation behavior of NR211–CL under swelling to investigate why there are differences in the plastic strain as a function of clearance height. As can be seen from the bulge shapes in Fig. 12, the NR211 and CL visually become thicker at lower clearance heights in the hydrated state. The thicknesses on the central and topside sections of the NR211 and CL at 100 RH% are summarized in Fig. 14. We note that in the case of an in-plane swelling of 12.7%, the thicknesses of the NR211 and CL become larger in accordance with a decrease in the clearance height. At an in-plane swelling of 5.0%, the CL thickness is similar to the value for the 25.0 μm clearance with an in-plane swelling of 12.7%. The strain components along the in- and through-planes at the central and topside section of the NR211 are shown in Fig. 15. The in-plane strain decreases with a decrease in the clearance height while through-plane strain increases. Whereas the in-plane strain for a 100 μm clearance is 0.23, the value for a 25 μm clearance is 0.015, which is less than one-tenth of the former value. On the contrary, the through-plane strain increases from 0.061 to 0.36 as the clearance height changes from 100 μm to 25 μm , which is a 6-fold increase. The NR211 could not freely swell in plane at lower clearance height, and this is the reason why the CL crack formation was delayed. The NR211 could easily swell more in the thickness direction than an unconstrained membrane which swells in all direction [32].

In a similar fashion, the strain components with an in-plane swelling ϵ_{in} of 5.0% are analyzed in Fig. 15. In spite of the larger clearance height of 100 μm , the in-plane strain is 0.085, which is less than half of the value for an in-plane swelling of 12.7%. These data lead us to the conclusion that CL crack formation can be delayed by regulating the changes in PEM dimension under hydration.

5.2. Mitigation methods to suppress CL crack formation

Any area on the CL with cracks causes both mechanical and chemical degradation of the PEM. During hydration and dehydration of the PEM, the part of the PEM located under the CL cracks is subjected to tensile stress [17]. Pinholes and tears occur in the PEM

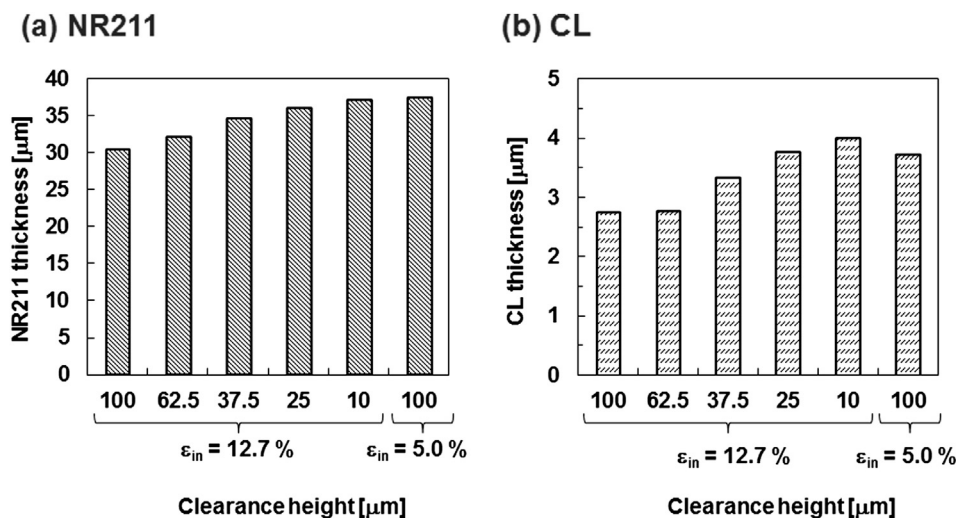


Fig. 14. Thicknesses at the central and topside portion of (a) NR211 and (b) CL at 100 RH% (swelled state).

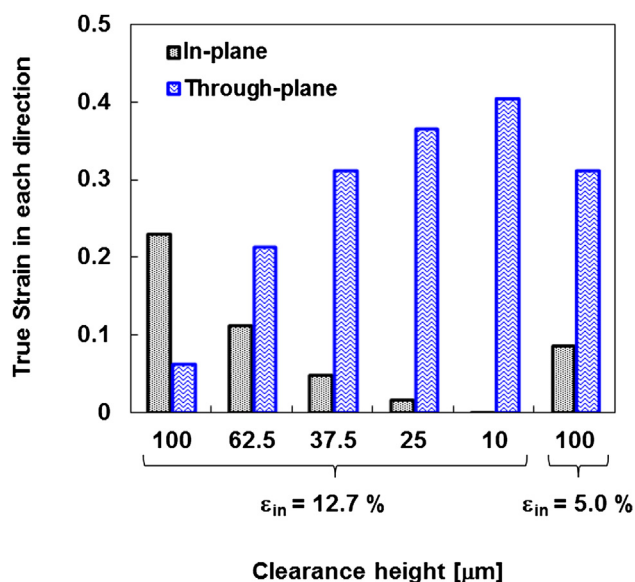


Fig. 15. Strain components at the central and topside portion of NR211 at 100 RH% (swelled state).

under the CL cracks [18]. Chemical degradation of the PEM portion under the CL cracks is accelerated. In dry conditions, gases such as H_2 or O_2 easily permeate into the cracks and generate radicals in the PEM or CL. Under wet conditions, radicals produced at the edges of the CL move into the bulk of the crack, which fills with liquid water [33]. These radicals accelerate chemical degradation of the PEM underneath the CL cracks. Hence, CL crack formation must be delayed to suppress PEM degradation.

Appropriate mechanical designs of the MEA, GDL and gas flow fields will promote longer resistance of the CL to crack formation. The mitigation methods to suppress CL crack formation can be proposed in terms of two mechanisms: external factors and internal factors.

With regard to external factors, secure contact between the MEA and GDL is essential. The GDL has a rough surface, and the surface concavity causes the deformation of the MEA [16,17]. The MPL coating on the GDL acts as a buffer layer to delay degradation of the MEA [19]. To prolong the MEA's lifetime further, compression of the concave MPL surface is required. Higher GDL rigidity [27] and narrower gas flow channels [10] are useful properties to better transmit compressive pressure from the GDL to the MEA under the channel of the gas flow fields.

Internal factors may also be proposed that serve to reduce the in-plane swelling of the PEM. The durability can be directly enhanced through improvements in the dimensional stability of the PEM. A reinforcement of the PEM effectively reduces the in-plane swelling [18], and one representative method of reinforcement is expanded PTFE (e-PTFE) [1,18,34–37]. By reducing the in-plane swelling ratio through reinforcement with e-PTFE, the new PEM exhibited a lifetime an order of magnitude longer than the reference PEM [18]. Correct design of the ePTFE reinforcement is critical to achieve durable composite membranes. Particularly, the increase in volume during swelling of the composite PEM should be equivalent to that of an ionomer monolayer to obtain better proton conductivity.

The mechanical properties of the CL are also important to resist cyclic loading. The ionomer content and its mechanical properties are key parameters related to crack formation resistance. Heat treatments can improve the mechanical properties by increasing the crystallinity of the ionomer [38].

In this paper, limited parameters were simulated, and the CL crack formation mechanism and proposals for mitigation methods were mainly considered. The plastic strain in the CL can be calculated as a function of several parameters: thickness, mechanical properties, swelling ratio of both the PEM and CL, and clearance height and width. By using simulations, CL crack formation was predicted under different durability conditions.

6. Conclusion

In this paper, experiments and FEM simulations were performed to address the issue of CL crack formation by bulge deformation under multiple humidity cycles. The formation of cracks in the CL was analyzed by performing buckling tests at several clearance heights. From the data of repeated humidity cycles, the CL cracks happen at the central and topside bulges, and the occurrence of cracks was reduced at lower clearance height. From the FEM analysis of the buckling tests, the higher plastic strain portion seen for the swollen state of the NR211–CL corresponds to the cracked CL portions in the experiment. The equivalent plastic strain in the CL decreases with a decrease in the clearance height. The mechanism that allows suppression of CL crack formation at lower clearance heights could be explained by analyzing the strain components of the NR211. When the NR211 swells, in-plane strain decreases with a decrease in the clearance height whereas through-plane strain increases. In the simulation of a modeled PEM with a low in-plane swelling ratio, the plastic strain in the CL was reduced.

To reduce the strain in the CL, lower clearance heights between the MEA and GDL and a lower in-plane swelling ratio in the PEM are recommended. A flat MPL, a rigid GDL and a narrow channel for the gas flow fields are useful methods to obtain lower clearance height. Lower in-plane swelling of the PEM can be achieved by alterations to the PEM composition such as reinforcement. Throughout this work, the mechanisms of MEA degradation and solutions to suppress the degradation under repeated humidity cycles were indicated.

Acknowledgments

The author wishes to express his gratitude to associates at Toyota Motor Corporation for their contributions via technical discussions, experiments and simulation support.

References

- [1] B. Kienitz, J. Kolde, S. Priester, C. Baczowski, M. Crum, *ECS Trans.* 41 (1) (2011) 1521–1530.
- [2] Y.-H. Lai, D.A. Dillard, in: W. Vielstich, H.A. Gasteiger, H. Yokokawa (Eds.), *Handbook of Fuel Cells, Advances in Electrocatalysis, Materials, Diagnostics and Durability*, vol. 5, John Wiley & Sons, Ltd., 2009, pp. 403–419.
- [3] Y.-H. Lai, C.K. Mittelsteadt, C.S. Gittleman, D.A. Dillard, *J. Fuel Cell Sci. Technol.* 6 (2009) 021002-1–021002-13.
- [4] Y. Li, D.A. Dillard, S.W. Case, M.W. Ellis, Y.-H. Lai, C.S. Gittleman, D.P. Miller, *J. Power Sources* 194 (2009) 873–879.
- [5] M. Pestrak, Y. Li, S.W. Case, D.A. Dillard, M.W. Ellis, Y.-H. Lai, C.S. Gittleman, *J. Fuel Cell Sci. Technol.* 7 (2010) 041009-1–041009-10.
- [6] Y. Li, D.A. Dillard, Y.-H. Lai, S.W. Case, M.W. Ellis, M.K. Budinski, C.S. Gittleman, *J. Electrochem. Soc.* 159 (2) (2012) B173–B184.
- [7] Y. Tang, M.H. Santare, A.M. Karlsson, S. Cleghorn, W.B. Johnson, *J. Fuel Cell Sci. Technol.* 3 (2006) 119–124.
- [8] A. Kusoglu, A.M. Karlsson, M.H. Santare, S. Cleghorn, W.B. Johnson, *J. Power Sources* 170 (2007) 345–358.
- [9] A. Kusoglu, M.H. Santare, A.M. Karlsson, S. Cleghorn, W.B. Johnson, *J. Electrochem. Soc.* 157 (5) (2010) B705–B713.
- [10] Z. Lu, C. Kim, A.M. Karlsson, J.C. Cross III, M.H. Santare, *J. Power Sources* 196 (2011) 4646–4654.
- [11] R. Solasi, X. Huang, Y. Zou, M. Feshler, K. Reifsnider, D. Condit, in: *ASME 4th International Conference on Fuel Cell Science, Engineering and Technology*, June 2006, Irvine, CA.
- [12] X. Huang, R. Solasi, Y. Zou, M. Feshler, K. Reifsnider, D. Condit, S. Burlatsky, T. Madden, *J. Polym. Sci. Part B Polym. Phys.* 44 (2006) 2346–2357.

- [13] R. Solasi, Y. Zou, X. Huang, K. Reifsnider, D. Condit, J. Power Sources 167 (2007) 366–377.
- [14] T.T. Aindow, J. O'Neill, J. Power Sources 196 (2011) 3851–3854.
- [15] M.N. Silberstein, M.C. Boyce, J. Power Sources 196 (2011) 3452–3460.
- [16] T. Uchiyama, M. Kato, T. Yoshida, J. Power Sources 206 (2012) 37–46.
- [17] T. Uchiyama, M. Kato, Y. Ikogi, T. Yoshida, J. Fuel Cell Sci. Technol. 9 (2012) 061005-1–061005-8.
- [18] W.K. Liu, S.J.C. Cleghorn, B.E. Delaney, M. Crum, in: W. Vielstich, H.A. Gasteiger, H. Yokokawa (Eds.), Handbook of Fuel Cells, Advances in Electrocatalysis, Materials, Diagnostics and Durability, vol. 5, John Wiley & Sons, Ltd., 2009, pp. 385–402.
- [19] A.B. LaConti, H. Liu, C. Mittlesteadt, R.C. McDonald, ECS Trans. 1 (8) (2006) 199–219.
- [20] G. Escobedo, K. Raiford, G.S. Nagarajan, K.E. Schwiebert, ECS Trans. 1 (8) (2006) 303–311.
- [21] M. Crum, W. Liu, ECS Trans. 3 (1) (2006) 541–550.
- [22] W. Liu, M. Crum, ECS Trans. 3 (1) (2006) 531–540.
- [23] S. Hommura, K. Kawahara, T. Shimohira, Y. Teraoka, J. Electrochem. Soc. 155 (1) (2008) A29–A33.
- [24] T. Madden, D. Weiss, N. Cipollini, D. Condit, M. Gummalla, S. Burlatsky, V. Atrazhev, J. Electrochem. Soc. 156 (5) (2009) B657–B662.
- [25] W. Yoon, X. Huang, J. Electrochem. Soc. 157 (4) (2010) B599–B606.
- [26] W. Yoon, X. Huang, ECS Trans. 33 (1) (2010) 907–911.
- [27] J. Kleemann, F. Finsterwalder, W. Tillmetz, J. Power Sources 190 (2009) 92–102.
- [28] Y.-H. Lai, Y. Li, J.A. Rock, J. Power Sources 195 (2010) 3215–3223.
- [29] F.E. Hızir, S.O. Ural, E.C. Kumbur, M.M. Mench, J. Power Sources 195 (2010) 3463–3471.
- [30] Y. Kai, Y. Kitayama, M. Omiya, T. Uchiyama, M. Kato, J. Fuel Cell Sci. Technol. 10 (2) (2013) 021007-1–021007-8.
- [31] F. Rong, C. Huang, Z.-S. Liu, D. Song, Q. Wang, J. Power Sources 175 (2008) 699–711.
- [32] A. Kusoglu, B.L. Kienitz, A.Z. Weber, J. Electrochem. Soc. 158 (12) (2011) B1504–B1514.
- [33] S. Kundu, M.W. Fowler, L.C. Simon, S. Grot, J. Power Sources 157 (2006) 650–656.
- [34] K.M. Nouel, P.S. Fedkiw, Electrochim. Acta 43 (1998) 2381–2387.
- [35] F.Q. Liu, B.L. Yi, D.M. Xing, J.R. Yu, H.M. Zhang, J. Membr. Sci. 212 (2003) 213–223.
- [36] S.-Y. Ahn, Y.-C. Lee, H.Y. Ha, S.-A. Hong, I.-H. Oh, Electrochim. Acta 50 (2004) 571–575.
- [37] J. Shi, B. Jang, J. Fuel Cell Sci. Technol. 8 (2011) 014501-1–014501-4.
- [38] J. Li, X. Yang, H. Tang, M. Pan, J. Membr. Sci. 361 (2010) 38–42.